Robotica (1999) volume 17, pp. 621–634. Printed in the United Kingdom © 1999 Cambridge University Press

Robotic assembly: chamferless peg-hole assembly

W. Haskiya, K. Maycock and J. Knight

Department of Mechanical and Manufacturing Engineering, De Montfort University, Leicester LE1 9BH (UK)
E-mail: whaskiya@dmu.ac.uk

(Received in Final Form: June 11, 1999)

SUMMARY
The peg-in-hole insertion process is the most common task in the robotic/automatic assembly industry. However, the inaccuracy of the assembly robot in positioning the inserted peg into the hole due to the uncertainty of the assembly environment, represents an obstacle in this area of automation. To overcome this problem, complex and expensive equipment has been designed. The objective of this paper is to provide an in-depth understanding of the chamferless peg-hole assembly, by showing the geometrical, dynamical conditions for a successful assembly operation. Also, the results of this analysis have been simulated to demonstrate the chamferless peg-hole insertion process.

KEYWORDS: Peg-in-hole; Geometrical analysis; Dynamical analysis; Simulation.

1. INTRODUCTION

A great deal of analysis of the peg-in-hole problem has been carried out in the past.[1–5] Our work describes the theoretical aspects that deal with the understanding of the relation between the mating parts throughout the insertion process (e.g. forces, moments, friction etc.),[6] or the practical aspects that deal with the equipment used to facilitate the insertion process (e.g. RCC wrists, different control strategies etc.).[7,8] Setchi et al.[9] have suggested a 3D simulation programme for the peg-in-hole insertion process. This approach considers the insertion process as a sequence of discrete events, and models the process as a transition from one contact situation to another. They also claim that this simulation is a tool for developing insertion strategies and devices for a specific application, such as chamferless mating parts. However, throughout the modelling stages it was assumed that the inserted peg is been supported by a compliant wrist device (RCC). This assumption contradicts the fact that RCC devices cannot accommodate positional errors between chamferless mating parts. This paper presents an investigation of the peg-in-hole insertion process. This investigation differs from others in that it adopts a passive accommodation approach and is still valid even in case when there is no chamfer on either of the mating parts.

2. PRELIMINARY ANALYSIS

This stage of the analysis provides the geometrical conditions of the peg and the hole for successful insertion in a 3-dimensional space, starting from initial stage where the peg is away from the hole. The peg's centre axis is tilted by ϑ about the Y axis, with respect to the Z axis, and the centre of the upper surface of the hole O_h is misaligned by e_x and e_y with respect to the centre of the peg tip O_p on the X_p-Y_p plane (Figure 1). Also, as shown in Figure 1 the vertical projection of the e_x, e_y from the X_p-Y_p plane on the X-Y plane is defined by $e_x \cos \vartheta$ and e_y, respectively.

By establishing a geometrical relationship between O_p and O_h the assembly stage is defined and its success or failure identified. Looking at the vertical projection of the peg tip over the hole it is seen that (Figure 2) to enable the peg to enter the mouth of the hole, the following conditions must be satisfied.

$$\begin{aligned} r\cos\vartheta + e_x \cos\vartheta \le R \\ r + e_y \le R \end{aligned} \tag{1}$$

from the X and the Y directions, consecutively. From eq. (1) the following relationships can be derived relative to the X axis:

$$\begin{aligned} \vartheta \le \cos^{-1}\left(\frac{R}{r+e_x}\right) \\ e_x \le \frac{R - r\cos\vartheta}{\cos\vartheta} \end{aligned} \tag{2}$$

and about the Y axis

$$e_y \le R - r \tag{3}$$

However, in the triangle OO_pO_h (Figure 2)

$$e_y = \tan\beta e_x \cos\vartheta \tag{4}$$

on condition that $e_x \cos \vartheta \neq 0$. Substitute eq. (3) into eq. (4)

$$\beta \le \tan^{-1}\left(\frac{R-r}{e_x \cos\vartheta}\right) \tag{5}$$

where β is the angular misalignment between the vertical projection of the tip centre of the peg (O_p) and that one of the hole (O_h) in the X-Y plane.

In equations (1) through (5), it can be noticed that a decrease in the clearance between the peg and the hole ($c = R - r$) will nullify the conditions given in those equations; therefore the peg will not enter the hole.

https://doi.org/10.1017/S026357479900185X Published online by Cambridge University Press

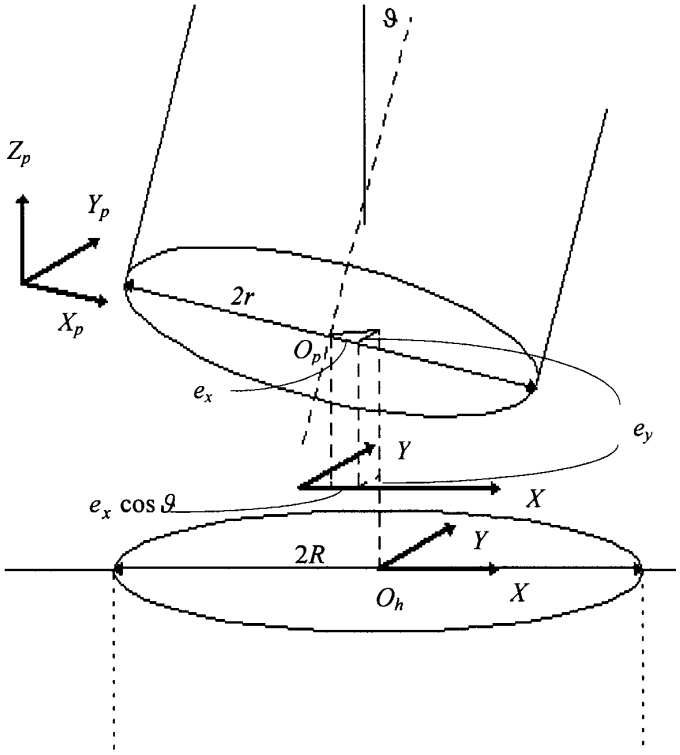


Fig. 1. Peg and a hole in 3D space.

However, an increase in the clearance will ease the insertion process, and satisfy the equations.

3. INVESTIGATION OF THE DYNAMIC OF 3D INITIAL CONTACT BETWEEN THE PEG AND THE HOLE

For ease of analysis, the following investigation is divided into 3 major stages:

3.1 Approach

The force balance of Figure 3 is,

$$\sum F = m(a-g) \tag{6}$$

$$v_i = \sqrt{2ah}$$

where v_i is the initial contact velocity when the peg contacts

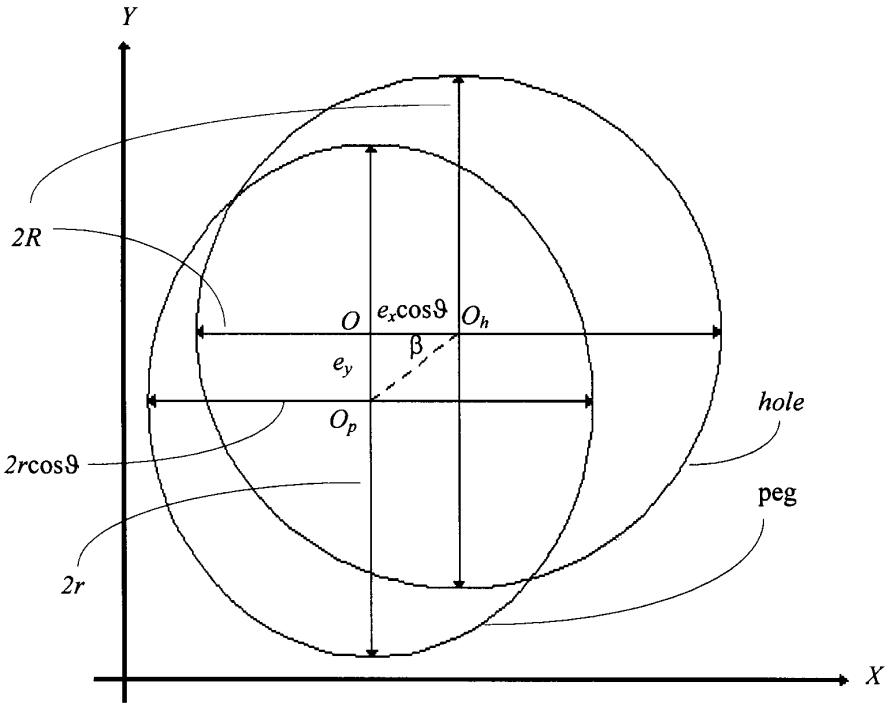


Fig. 2. Vertical projection of the peg tip over the hole.

https://doi.org/10.1017/S026357479900185X Published online by Cambridge University Press

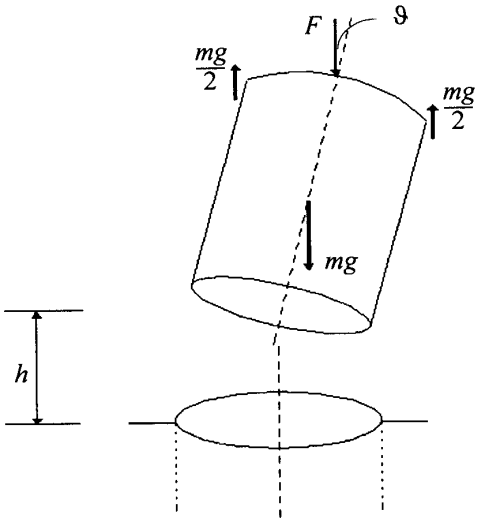


Fig. 3. Approach stage.

the hole surface, m is the peg mass, and h is the distance before the peg contacts the hole. In eq. (6) the acceleration a is constant; it is assumed there is no relative movement between the gripper (gripping force) and the peg.

It can be seen that in eq. (6), the relationship between the insertion force and the insertion velocity is proportional, which means that any change in either value will affect the outcome of the next stage.

3.2 Initial contact between the peg and the surface of the hole

The investigation of this section will provide an analysis for predicting slipping or sticking and the possible 3 points of contact between the peg and the hole.

3.2.1. Slipping or sticking. The contact modes between the peg and the upper surface of the hole are determined by factors such as the friction and its inconsistency, effect of impact and the conservation of energy etc. Although the last two phenomena are beyond the scope of this investigation, it is worth to mention here some other work in this area. Mason and Wang[10] propose a thorough investigation of impact model for removing frictional inconsistency. Also Featherstone[11] address the impact inconsistency in the presence of friction. For the representation of friction in 3D space and also energy conservation, see Erdman.[12]

Thus, the goal of our investigation is to determine the outcome mode (sticking/slipping) after the initial contact between the peg and the upper surface of the hole. To simplify the analysis, it is assumed that the coefficient of friction is static and constant between the peg and the hole. Also, it is assumed that the forces during the collision (contact) are impulsive $\mathbf{F}_{imp}$ because of their large magnitude.

As shown in Figure 4, there are two points of contact in which are affected by impulsive forces. In the 3D space it is convenient to choose the reference point of an impulsive force for an object (peg) at its centre of mass (COM). Now, it is possible to use Coulomb's law of a friction/friction cone to determine whether sticking or slipping will occur. Points

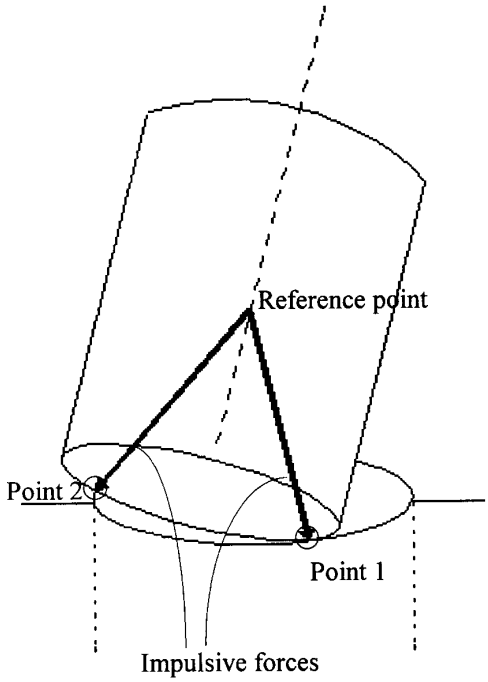


Fig. 4. Initial contact between the peg and the upper surface of the hole.

(1, 2) of Figure 4 are acted upon by an equal impulsive force. Therefore the analysis will concentrate on just point (1), and the outcome will be correct for point (2) as well. The configuration space of the impulsive force acing on point (1) is as follows (Figure 5): In Figure 5, and at point (1), the reaction force f_r is the sum of the normal force f_n and the friction force f_t. In the same Figure it can be seen that the impulsive force emerges from the friction cone which means that the peg will slide along the constrained surface of the hole (tangential to the contact point). Also, it is seen that the impulsive force and the reaction force have to lie in the same plane. Hence,

$$\begin{aligned} \mathbf{J} &= \int \mathbf{F}_{imp}\, dt \text{ or,} \\ \mathbf{J} &= m\mathbf{v}_f + m\mathbf{v}_i \text{ and,} \\ \mathbf{J} &= \Delta\mathbf{P} = \mathbf{P}_f - \mathbf{P}i \end{aligned} \tag{7}$$

where $\mathbf{J}$ is the impulse of the force or the change in momentum ($\Delta\mathbf{P}$), $\mathbf{v}_f$ and $\mathbf{v}_i$ are the final velocity after the break of contact and the initial velocity; dt is the duration of

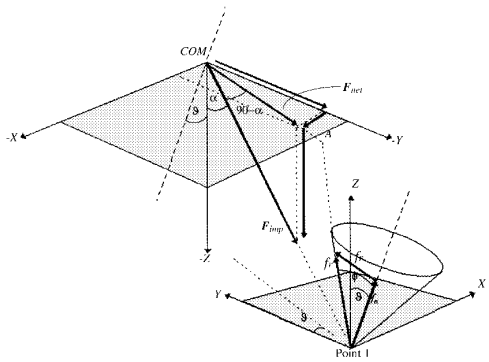


Fig. 5. 3D space of point (1) and the impulsive force acting upon.

https://doi.org/10.1017/S026357479900185X Published online by Cambridge University Press

the contact. Since this duration is too short ($\Delta t \Rightarrow 0$), *dt* is used; then the rearranged eq. (7) will yield eq. (8),

$$\mathbf{F}_{imp} = \frac{\Delta \mathbf{P}}{dt} = \frac{m(v_f - v_i)}{dt}$$
$$\mathbf{F}_{imp} = ma_f \tag{8}$$

where a_f is the breaking acceleration from the sticking to the slipping stage. A comparison between eq. (6) and eq. (8) will show that the difference between the two forces involved is the acceleration, where in eq. (6) the acceleration is constant, but in eq. (8) is not, though it is large enough to overcome and break the contact between the peg and the top surface of the hole. In regard to point (2), the magnitude of the impulsive force is half of that in eq. (8), which is equal to that acting on point (1).

In a general case, to determine the contact mode, one considers the plane (COM, A, point 1) of Figure 5; it can be said that (eq. 9),

$$\begin{aligned} &\mathbf{F}_{imp} - f_r = \mathbf{F}_{net} \text{ which is slipping, but if} \\ &\mathbf{F}_{imp} - f_r = \text{Othen the peg is on the verge of slipping, for} \\ &\mathbf{F}_{imp} \langle f_r \text{ the peg will stick.} \end{aligned} \tag{9}$$

To conclude the investigation of the peg-hole contact mode of this stage of the assembly, consider Figure 5; this shows the contact mode conditions (Table I).

3.2.2 The possibility of three points of contact (3 POC). When using compliant devices, such as the RCC, for inserting a peg into a hole, it is hard to cope with three points of contact between the mating parts due to the insufficient compliance of the wrist about the insertion axis,

Table I: Contact mode conditions

Slipping	Verge of slipping	Sticking
$\vartheta \langle (\pi/2 - \phi)$ or $\vartheta + \alpha \rangle \phi$	$\vartheta = (\pi/2) - \phi$ or $\vartheta + \alpha = \phi$	$\vartheta \rangle (\pi/2) - \phi$ or $\vartheta + \alpha \langle \phi$
$(\tan\phi \ \ \mu)$*	$(\tan\phi = \mu)$*	$(\tan\phi \ \ \mu)$*

* Refer to the friction cone section.

where the need for rotation and motion to overcome this mode of contact is greater than in the other phases of the assembly. Hence, the goal is to avoid having a 3 POC situation. Such a mode of contact is a geometrical relation rather than a force/moment relation; hence, the identification of the variables (Angular error, lateral error etc.) during that stage of the insertion process will facilitate the design of an assembly task for avoiding this mode of contact.

As shown in Figure 6, the peg is in contact with the hole at 3 different points, and this satisfies $d/\cos\vartheta$ larger than *D*, where *d* and *D* are the peg and the hole diameters, and ϑ is the angular misalignment between the peg and the hole. To avoid 3 points of contact, the following relation must be satisfied:

$$\frac{d}{\cos\vartheta} \le D \tag{10}$$

which means that the reaction forces at point (1) and or point (2) must be zero. In regard to the reaction at point (3), this will exist until the one or two point of contact break and the peg slides down the hole.

The clearance between the peg and the hole is $c = R\text{-}r$; putting this relation in eq. (10) will give the maximum allowable clearance to avoid 3 POC (eq. 11),

$$c \ge \frac{(1 - \cos\vartheta)r}{\cos\vartheta} \tag{11}$$

in Figure 6, the top view is the projection of the peg's tip over the mouth of the hole; to avoid a 3 POC situation, the $d/\cos\vartheta$ must be either smaller or equal to *D*. In the first case,

$$e_x = R - \frac{r}{\cos\vartheta} \tag{12}$$

This is the allowable lateral error along the X axis which will not cause the 3POC problem. Substitute $c = R\text{-}r$ in eq. (12)

$$\vartheta = \cos^{-1}\left(\frac{r}{r + c + e_x}\right) \tag{13}$$

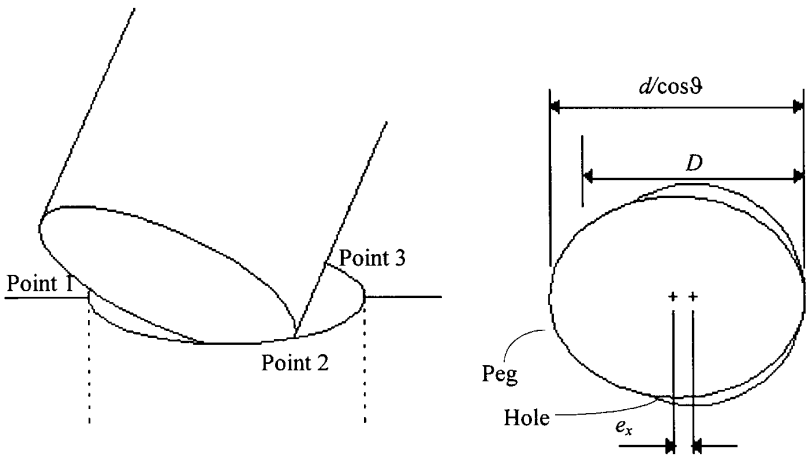


Fig. 6. Peg is in 3 point of contact with the hole.

https://doi.org/10.1017/S026357479900185X Published online by Cambridge University Press

and in the second case where $e_x = 0$, the

$$\vartheta = \cos^{-1}\left(\frac{r}{r+c}\right) \tag{14}$$

Both equations (13 and 14) give the range of admissible angular error in which it can be accommodated and the 3 POC problem avoided.

3.2.3 The ideal wrist stiffness.. The equilibrium equations that describe the peg sliding in during the 3 POC mode, assuming that the peg is moving at a uniform velocity (Figure 7), are then given by

$$F_Z = 2f + \mu f_3 (f = f_1 = f_2) \tag{15}$$

$$F_X = 2\mu f + f_3 \tag{16}$$

$$M_3 = F_Z r + F_X l \tag{17}$$

Where the F_x is the lateral force which is a result of the lateral stiffness of the wrist. Substitute eq. (15) into eq. (16)

$$f_3 = \frac{F_X - \mu F_Z}{1 - \mu^2} \tag{18}$$

Equalizing eq. (17) to the moment where the peg is rotating (centre of rotation, point O of Figure 7)

$$F_Z r + F_X l = \left(\frac{F_X - \mu F_Z}{1 - \mu^2}\right)(l + \mu r) \tag{19}$$

Solving eq. (19) will give the relation between the insertion and the lateral forces (eq. 20)

$$\frac{F_X}{F_Z} = \frac{1}{\mu} \tag{20}$$

Considering both the compliant wrist and the inserted peg as one object during the 3 POC mode (Figure 7), the moment in the wrist is equal to a moment anywhere on the peg. Now, to find the optimum stiffness (ideal) that will enable the wrist to overcome the 3 POC mode, we equalize the moment at the wrist with that at the third contact point between the peg and the hole; then

$$K_X(e_{x_0} - e_x)L_g - K_\vartheta(\vartheta - \vartheta_0) = F_Z r + F_X l \tag{21}$$

where L_g is the centre of rotation or the distance from the wrist to the point in space where the peg rotates.
also,

$$K_X(e_{x_0} - e_x) = -F_X \tag{22}$$

Substitute eq. (20 and 22) into eq. (21)

$$-|K_\vartheta| = \frac{\frac{F_Z}{\mu}(L_g + \mu r + l)}{\vartheta - \vartheta_0} \text{ or } -|K_\vartheta| = \frac{F_X(L_g + \mu r + l)}{\delta\vartheta} \tag{23}$$

where $\delta\vartheta = \vartheta - \vartheta_0$
The ideal lateral wrist stiffness, can be found from the

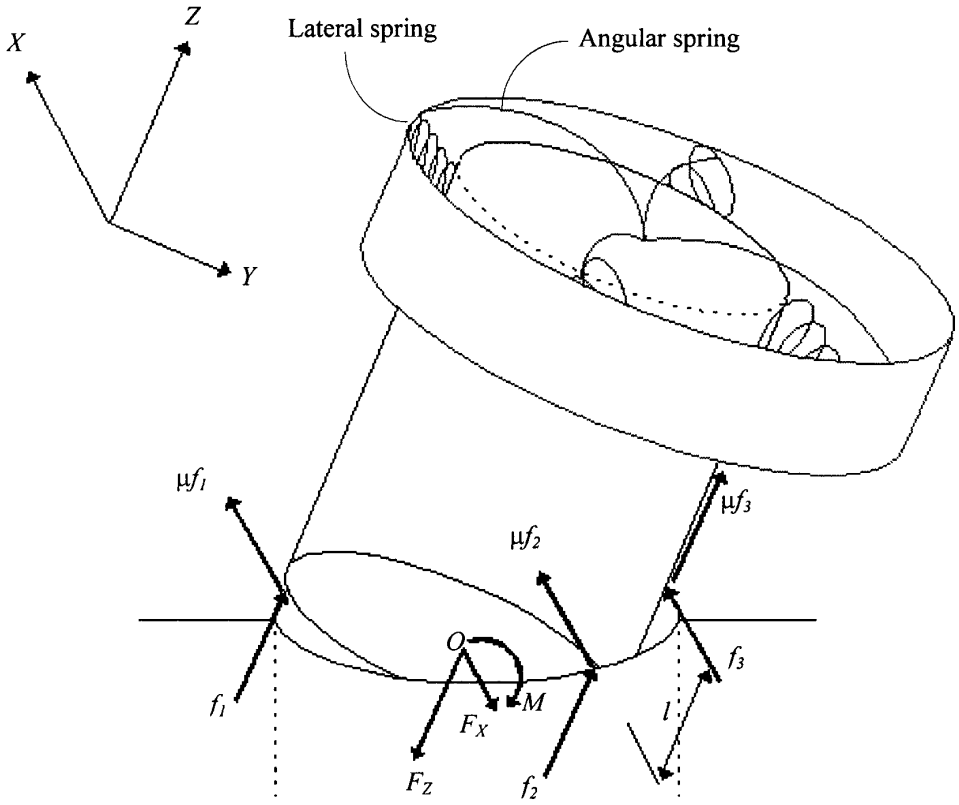


Fig. 7. Schematic of peg-wrist during 3POC.

https://doi.org/10.1017/S026357479900185X Published online by Cambridge University Press

relation (eq. 22)

$$K_X = \frac{-F_X}{\delta e_x} \quad \text{or}$$

$$K_X = \frac{-\frac{F_Z}{\mu}}{\delta e_x} = -\frac{F_Z}{\mu\,\delta e_x} \tag{24}$$

where $\delta e_x = e_{x_o} - e_x$

Both equations (23 and 24) give the ideal wrist stiffness to overcome the 3 POC mode. Note, that the δe_x and the $\delta\vartheta$ correspond to those displacements of the peg, and they are equal.

3.3 Peg is inside the hole: the conditions for successful assembly

Once the wrist-peg overcomes the 3 POC mode, the peg will either slide in or will contact the hole in a one/two-point contact which may cause jamming or wedging if proper conditions are not met.

Jamming[13] is defined as a condition in which the peg will not move during the insertion action, because the forces and moments applied to them through the supports are in the wrong proportions. Consequently, jamming could occur during both the one and two point contact. To overcome jamming, the direction of the insertion force must be changed so that the resultant force can lie outside the friction cone. This is achieved by removing the peg from the hole and changing its orientation and then reinserting it into the hole.

Wedging[13] is a condition in which the reaction forces are inside their friction cones and act along the same line; thus movement cannot occur. Wedging is worse than jamming because the removal of the insertion force will not remove the reaction forces. Unlike jamming, the cause is geometric rather than ill-proportioned forces. Wedging occurs when the insertion depth (during the two-point contact) is smaller than the coefficient of friction times the peg diameter ($l_2 < \mu d$). Also, the tilt angle should be smaller than the ratio clearance over coefficient of friction ($\vartheta < c/\mu$).

Now, to determine whether an assembly will succeed or fail, it is necessary to consider the forces acting on the parts. Also, it is assumed that the friction is consistent all over between the peg and the hole. In Figure 8, the peg is in equilibrium conditions and slides down the hole at a uniform velocity; it is assumed that the angle of tilt between the peg and the hole is zero. It is seen from Figure 8 that the possible contact modes could be any of those of Table II.

Table II: Possible contact modes

One-point Contact	Two-point Contact	Line Contact
P_1	P_1 & P_2	P_1 & P_2
P_2	P_4 & P_3	P_4 & P_3
P_3	P_1 & P_3	
P_4	P_4 & P_2	
		P_1 & P_2 & P_4 & P_3

Where P_2, P_2, P_3 and P_4 are points of contact. In this analysis the situation of P_1 & P_2 & P_4 & P_3 will not be dealt with because it is a circular contact (interference fit) which occurs when the peg is completely inside the hole, or at the completion of a successful assembly process. Starting with the two-point contact, then the equilibrium equations that describe the peg sliding in during P_1 & P_3 (Figure 9) are then given by:

$$\begin{aligned} F_X &= f_3 - f_1 \\ F_Z &= \mu(f_1 + f_3) \\ M &= f_1 l - \mu r(f_3 - f_1) \end{aligned} \tag{25}$$

solving eq. (25) leads to

$$\frac{M}{rF_Z} = \frac{l}{2r\mu} - \frac{F_X}{F_Z}\left(\frac{l}{2r} + \mu\right) \tag{26}$$

So far the tilt angle has been ignored ($\vartheta = 0$). But if the tilt angle is not zero, then as in Figure 10 the X-Z axes are tilted by ϑ, and the rotational displacement of the peg is denoted by (s), which the peg makes with respect to the hole (in radians it is $s = \vartheta r$). Theoretically, point (O) from Figures 8 and 9 will remain in the same position even after the tilt (Centre of rotation is at the peg tip). Therefore the change in the moment about point (O) can be expressed in terms of s and ϑ in place of r.

Then put $r = \frac{s}{\vartheta}$ into eq. (26),

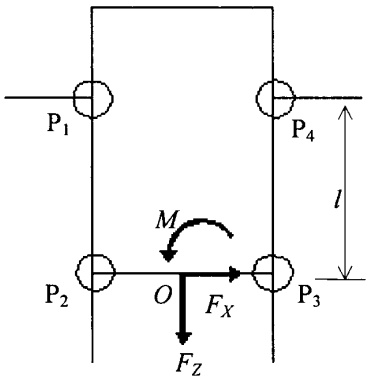


Fig. 8. Peg is inside the hole tilt angle is zero.

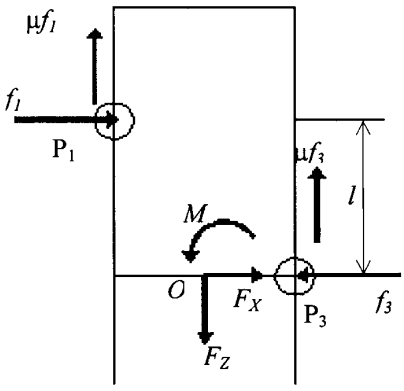


Fig. 9. Peg in two-point contact ($\vartheta = 0$).

https://doi.org/10.1017/S026357479900185X Published online by Cambridge University Press

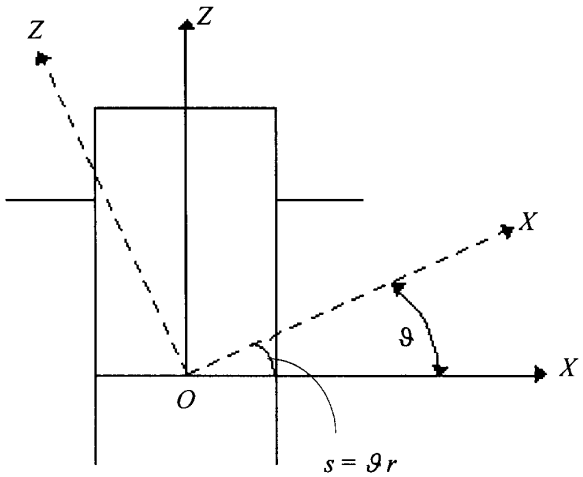


Fig. 10. Centre axis of peg is tilted by ϑ.

$$\frac{M\vartheta}{sF_Z} = \frac{\vartheta l}{2s\mu} - \frac{F_X}{F_Z}\left(\frac{\vartheta l}{2s} + \mu\right)$$

$$\frac{M\vartheta}{F_Z} = \frac{\vartheta l}{2\mu} - \frac{F_X}{F_Z} \times \frac{\vartheta l}{2} - \frac{F_X}{F_Z} \times \mu s \tag{27}$$

$$\frac{M\vartheta}{F_Z} = \frac{l\vartheta}{2\mu} - \frac{F_X}{F_Z}\left(\frac{l\vartheta}{2} + \frac{\mu s}{1}\right)$$

Define

$$\lambda = \frac{l\vartheta}{2\mu} \tag{28}$$

then. eq (27) can be expressed as

$$y = mx + b \tag{29}$$

which is a straight line, where

$$y = \frac{M\vartheta}{F_Z}$$

$$x = \frac{F_X}{F_Z}$$

$$m = -\mu(\lambda + s) \tag{30}$$

$b = \lambda$ and if the peg was tilted to the other side then

$b = -\lambda$

To finish the derivation one must consider all the possible contact modes, half of which will suffice for illustration.

For the contact mode P_1 and P_2 Figure 11. The equilibrium equations are

$$F_X = -f$$

$$F_Z = \mu f = -\mu F_X \tag{31}$$

$$\frac{F_X}{F_Z} = -\frac{1}{\mu}$$

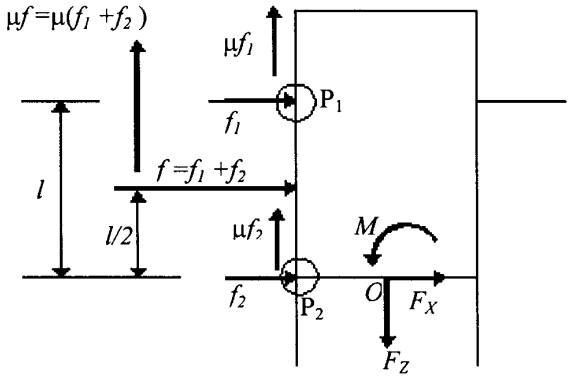


Fig. 11. Peg is in line contact with the hole.

and

$$M = f\left(\frac{l}{2} + \mu r\right) = -F_X\left(\frac{l}{2} + \mu r\right) \tag{32}$$

When tilting the peg by ϑ, the line contact between the peg and the hole becomes a one-point contact, either P_1 or P_2, which depends upon the direction of the tilt. In eq. (32), the insertion depth $l/2$ becomes l; put $r = \frac{s}{\vartheta}$ into eq. (32)

$$M = -F_X\left(l + \mu \times \frac{s}{\vartheta}\right)$$

$$\frac{M\vartheta}{F_Z} = -\frac{F_X}{F_Z} \times \vartheta\left(l + \mu \times \frac{s}{\vartheta}\right) \tag{33}$$

$$\frac{M\vartheta}{F_Z} = +\frac{1}{\mu}(l\vartheta + \mu s)$$

$$\frac{M\vartheta}{F_Z} = 2\lambda + s$$

and for the other side of the peg (P_3 and P_4), one should obtain

$$\frac{F_X}{F_Z} = \frac{1}{\mu} \quad \text{and}$$

$$\frac{M\vartheta}{F_Z} = -(2\lambda + s) \tag{34}$$

For the one-point contact mode (P_1) the equilibrium equations are (Figure 12)

$$F_X = -f_1$$

$$F_Z = \mu f_1 = -\mu F_X \tag{35}$$

$$\frac{F_X}{F_Z} = -\frac{1}{\mu}$$

and

https://doi.org/10.1017/S026357479900185X Published online by Cambridge University Press

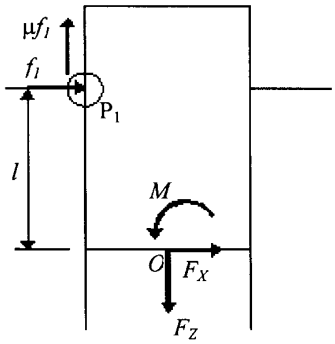


Fig. 12. Peg is in one-point contact.

$$M = f_1(l + \mu r) = -F_X(l + \mu r) \tag{36}$$

Tilt the peg by ϑ, then substitute $r = \frac{s}{\vartheta}$ into eq. (36)

$$M = -F_X\left(l + \mu \times \frac{s}{\vartheta}\right)$$

$$\frac{M\vartheta}{F_Z} = -\frac{F_X}{F_Z} \times \frac{l\vartheta}{1} - \frac{F_X}{F_Z} \times \frac{\vartheta \mu s}{\vartheta}$$

$$\frac{M\vartheta}{F_Z} = -\frac{F_X}{F_Z}(l\vartheta + \mu s) \tag{37}$$

$$\frac{M\vartheta}{F_Z} = \frac{1}{\mu}(l\vartheta + \mu s)$$

$$\frac{M\vartheta}{F_Z} = \frac{l\vartheta}{\mu} + s$$

$$\frac{M\vartheta}{F_Z} = 2\lambda + s$$

and for the other one-point contact (P_4), one should obtain

$$\frac{F_X}{F_Z} = \frac{1}{\mu} \text{ and}$$
$$\frac{M\vartheta}{F_Z} = -(2\lambda + s) \tag{38}$$

Now, for the bottom one-point contact (P_2) Figure 13, the equilibrium equations are

$$F_X = -f_2$$
$$F_Z = \mu f_2 = -\mu F_X$$
$$\frac{F_X}{F_Z} = -\frac{1}{\mu} \tag{39}$$

and

$$M = \mu f_2 r = -\mu r F_X \tag{40}$$

Tilt the peg by ϑ, then substitute $r = \frac{s}{\vartheta}$ into eq. (40)

$$M = -\mu \frac{s}{\vartheta} F_X$$

$$\frac{M\vartheta}{F_Z} = -\mu s \times \frac{F_X}{F_Z} \tag{41}$$

$$\frac{M\vartheta}{F_Z} = s$$

and for the other one-point contact (P_3), one should obtain

$$\frac{F_X}{F_Z} = \frac{1}{\mu} \text{ and}$$
$$\frac{M\vartheta}{F_Z} = -s \tag{42}$$

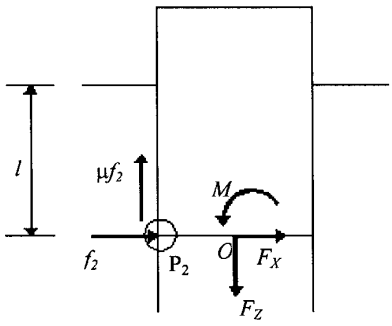


Fig. 13. Peg is in one-point contact from the bottom.

The results of this analysis are summarised in Figure 14. The jamming parallelogram's may be interpreted as follows: The combination of F_x, F_z and M falling on the parallelogram's edges describes the sliding in. Outside the parallelogram lies a combination which jams the peg either in the one (which is unlikely to happen during assembly operation) or two-point contact. Inside, the peg is in disequilibrium sliding or falling in. Note that the vertical dotted lines (points P_1 & P_2, P_3 & P_4) describe a line contact.

Also, as λ approaches zero, that is, the insertion depth is small compared to the radius of the peg, the parallelogram collapses to a line from $1/\mu$ (s on the right) to $-1/\mu$ (s on the left). Thus the initiation of a two-point contact, the no-jam region is quite small, and the possibility of jamming is high. Jamming is most likely to occur during insertion tasks with very small tolerances, because the smaller the tolerances, the smaller the insertion depth at which two-point contact occurs. When the peg is deep inside the hole, λ approaches infinity, and the parallelogram expands to a vertical strip lying between $-1/\mu$ and $1/\mu$, implying that one-point contact jamming is possible, but two-point contact jams are difficult to achieve.

4. PEG-HOLE MODELLING

It is assumed that the insertion process is subject to a mixture of viscous and friction damping. The viscous effect is negligible because of the low air resistance to the insertion process. Although friction damping has an important role in this process, it is beyond the scope of this work.

https://doi.org/10.1017/S026357479900185X Published online by Cambridge University Press

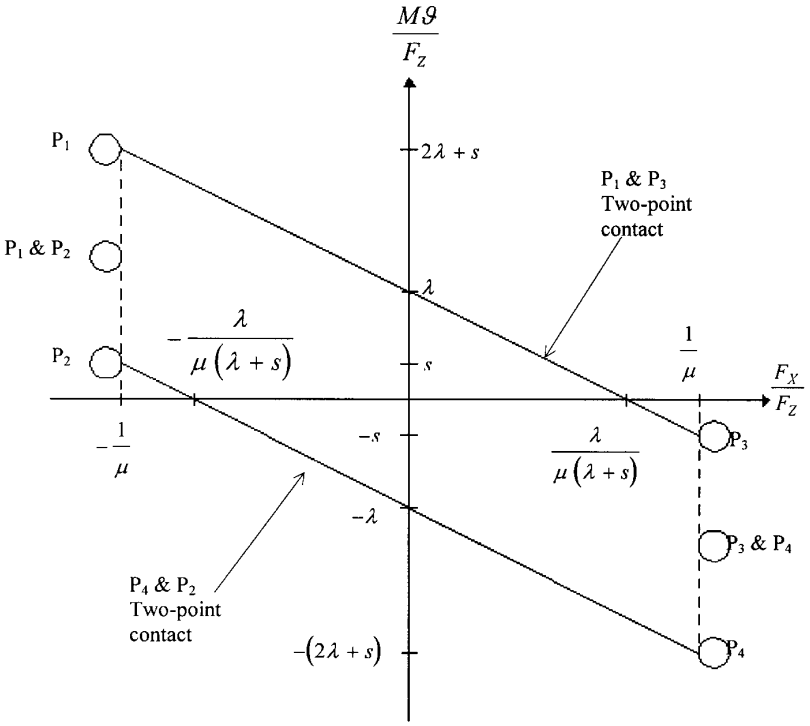


Fig. 14. The jamming diagram (after Whitney).

References 11 and 12 contain a thorough discussion of friction effects. In this paper, the friction is considered to be constant.

In this model the insertion process is treated as a 3D problem until the peg enters the hole (one/two-point contact). Whereas the contact between the peg and the hole occurs just in one plane, the problem is reduced to a 2D space. Also, note that the co-ordinate axes system of the peg and that of the hole are in the same plane. Now, the insertion process is divided into sub-processes where each sub-process occurs independently. In some of the sub-processes, the input is the output of the previous process.

Figure 15 shows a block diagram for the insertion process. The pneumatic piston applies a constant force that drives the peg downward. If there is misalignment, reaction forces will arise and cause the springs to deflect. This deflection is fed to the summing point in the form of a reaction force to accommodate the misalignment. The process is repeated until the peg is completely inside the hole.

5. MODELLING STAGES

In this section, the insertion process is divided into 5 sub-processes:

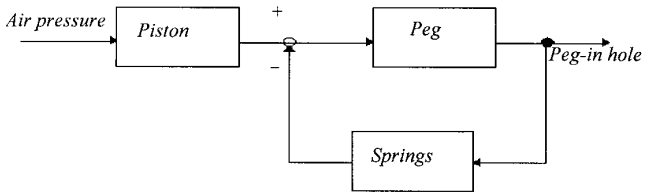


Fig. 15. General block diagram of the insertion process.

5.1 Approach Stage

As shown in Figure 16, it is assumed that the peg is above the hole and there are no positional misalignments.

The output z is the distance the peg has to travel to get into the hole. This stage is described by the differential equation:

$$F_{in(t)} = m\frac{d^2z}{dt^2} \tag{43}$$

To find the output z, eq. (1) can be expressed by a Laplace transform yielding:

$$\begin{aligned} F_{in(s)} &= ms^2 Z_{(s)} \\ Z_{(s)} &= F_{in(s)}\frac{1}{ms^2} \end{aligned} \tag{44}$$

The simulation block diagram describes this insertion process (Figure 17).

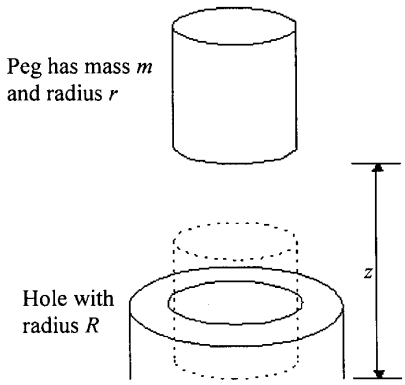


Fig. 16. A one stage insertion process (no misalignments).

https://doi.org/10.1017/S026357479900185X Published online by Cambridge University Press

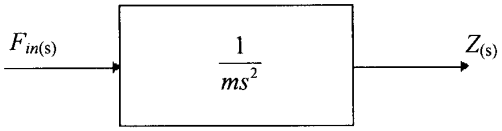


Fig. 17. A simulation block diagram for peg-hole (no misalignments).

On the other hand, when there is an initial lateral misalignment between the peg and the hole, it will result in a reaction force during the approach contact which causes the spring K_z to compress (Figure 18). The output z will be the vertical distance from the bottom surface of the peg to the upper surface of the hole.

5.2 Initial Contact

Figure 18 shows the peg-wrist during the initial, angular misalignment contact with the hole. The springs represent the compliant wrist. The reaction force generates a torque that tilts the peg into the mouth of the hole.

Note that in the 3D space, during the contact between the bottom of the peg and the top of the hole, the springs will react in one plane (either the X-Z or the Y-Z plane), despite the fact that the system has 6 degrees of freedom (3 transitional and 3 rotational).

In Figure 18, the lateral springs have lateral stiffness of K_x, K_y and K_z which are equal, and rotational stiffnesses of $K_{\vartheta X}$, $K_{\vartheta Y}$, and $K_{\vartheta Z}$, which are also equal. Note that in this sub-process only two rotational springs will provide the torque to tilt the peg, either $K_{\vartheta X}$ and $K_{\vartheta Z}$, or $K_{\vartheta Y}$ and $K_{\vartheta Z}$. Also, their angular deflection is in the same plane and direction. The dynamic differential equation that describe this sub-process is,

$$T_{(t)} = I\frac{d^2\vartheta}{dt^2} + (K_{\vartheta X}\,\vartheta + K_{\vartheta Z}\,\vartheta) \qquad (45)$$

$$T_{(t)} = I\frac{d^2\vartheta}{dt^2} + 2K_{\vartheta}\,\vartheta \text{ since } K_{\vartheta X} = K_{\vartheta Z}$$

The output ϑ is the angular deflection of the springs which

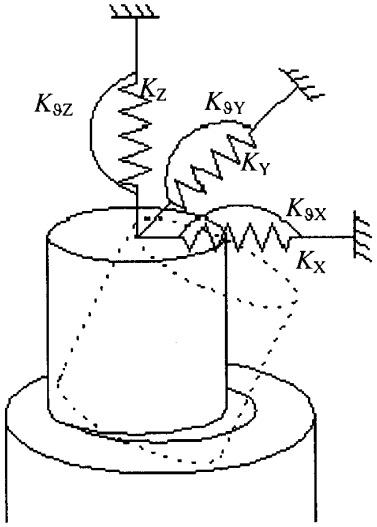


Fig. 18. The initial contact sub-process.

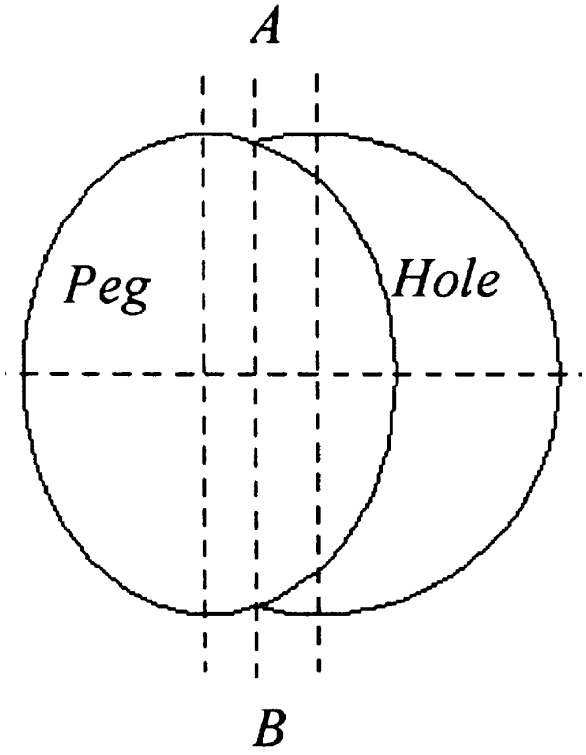


Fig. 19. Projection of the peg surface over the mouth of the hole.

corresponds to the angular error between the mating parts. $d^2\vartheta/dt^2$ is the angular acceleration and I is peg moment of the inertia which is equal to ($mr^2/2$), and T is the reaction torque at the contact point between the peg and the hole. In Figure 19 the projection of the peg over the mouth of the hole shows that the line AB connecting the two points of contact between the peg and the hole crosses the distance between the centre of the hole and that of the peg equally. This assumes that the angle of tilt is small (normally less than 5°). The reaction torque is given by:

$$T = F_Z \times \frac{e_x \cos\vartheta}{2} \qquad (46)$$

To find the output ϑ, the system differential equation (eq. 3) can be expressed by the Laplace transform method. Then,

$$T_{(s)} = Is^2\vartheta + 2K_{\vartheta}\vartheta$$
$$T_{(s)} = \vartheta(Is^2 + 2K_{\vartheta}) \qquad (47)$$
$$\vartheta_{(s)} = T_{(s)}\frac{1}{Is^2 + 2K_{\vartheta}}$$

and the simulation diagram that describes this equation is shown in Figure 20.

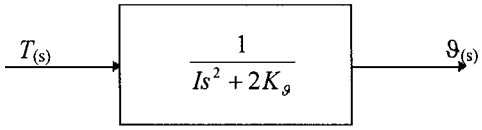


Fig. 20. A simulation block diagram for the peg initial tilt.

https://doi.org/10.1017/S026357479900185X Published online by Cambridge University Press

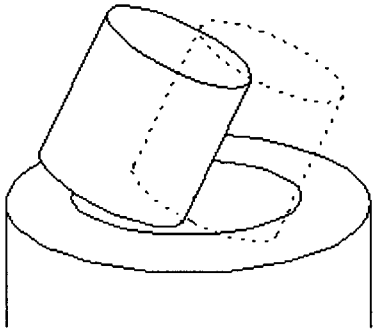


Fig. 21. Peg is moving to the far side of the hole (transitional).

5.3 Transition Stage

At this stage the peg moves to the far side of the hole (Figure 21), by e_x (output), which corresponds to the spring K_x compression (of Figure 18).

Note that the forces that move the peg are generated by the compression of another spring (because of the double sponge systems) and act in the same direction of the peg movement. The forces acting on the free body diagram (FBD) of the peg are shown in Figure 22,

The dynamic equation describing this system is

$$F_X = ma + F_S + f_t \tag{48}$$

where the input F_x is the lateral force and equal to $2K_xe_x$ because of the double spring system (sponge); F_s is the spring force, and the f_t is the friction force. Note that

$$f_t = \mu f_n = \mu F_Z = \mu^2 F_X \tag{49}$$

where f_n is the normal force. Rearranging eq. (48), and putting eq. (49) into it

$$\begin{aligned} F_{X(t)} &= m\frac{d^2e_x}{dt^2} + K_X e_x + \mu^2 F_{X(t)} \\ F_{X(t)} &= \frac{1}{1-\mu^2}\left(m\frac{d^2e_x}{dt^2} + K_X e_x\right) \end{aligned} \tag{50}$$

Expressing the system differential equation by the Laplace transform method for a zero initial condition,

$$\begin{aligned} F_{X(s)} &= \frac{1}{1-\mu^2}(ms^2 e_x + K_X e_x) \\ e_{x(s)} &= F_{X(s)}\frac{1-\mu^2}{ms^2 + K_X} \end{aligned} \tag{51}$$

The simulation diagram for this stage is shown in Figure 23.

However, if the peg approaches the hole with an initial

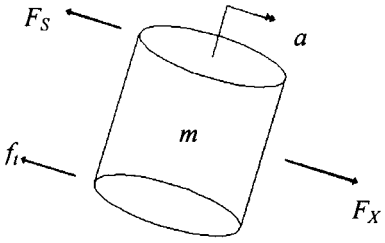


Fig. 22. The FBD of the peg during the transition stage.

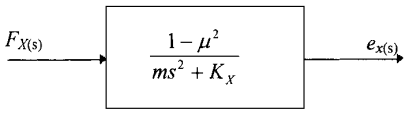


Fig. 23. Simulation block diagram for the peg transitional stage.

angular misalignment from the left-side (Figure 24), then during contact between the mating parts, the input is the torque generated from the reaction forces and the output is ϑ.

Note that to accommodate this misalignment, the springs will react in one plane, either rotational springs $K_{\vartheta Z}$ and $K_{\vartheta X}$ or $K_{\vartheta Z}$ and $K_{\vartheta Y}$. The differential equation that describes this stage is

$$\begin{aligned} T_{(t)} &= I\frac{d^2\vartheta}{dt^2} + (K_{\vartheta X}\,\vartheta + K_{\vartheta Z}\,\vartheta) \\ T_{(t)} &= I\frac{d^2\vartheta}{dt^2} + 2K_\vartheta\,\vartheta \end{aligned} \tag{52}$$

Which is the same as eq. (45), except that ϑ is on the other side, and the torque is

$$T = F_Z \times r \times \cos^2\vartheta \tag{53}$$

5.4 Transition From One To Two-Point Contact

The next stage is where the peg slides down the hole and two-point contact occurs (Figure 25). In fact, this is a stage continuous to the one before.

In this stage the insertion system will continue in providing the peg with the vertical motion (sliding-in) while maintaining the one-point contact with the hole until a stage is reached where the reaction forces cause the peg to change from one- to a two-point contact mode.

The forces acting on the FBD of the peg are shown in Figure 26. Note that the line of action of all forces lies in one plane; this reduces the 3D problem to a 2D problem.

The following equation is derived from Figure 26:

$$F_{in} - F_Z - \mu f_1 = ma \tag{54}$$

Also, the following relations exist:

$$\begin{aligned} &f_1 = F_X \quad \text{FBD of peg without springs,} \\ &\frac{F_X}{F_Z} \le \frac{1}{\mu} \quad \text{and,} \\ &F_X = K_X e_x \end{aligned} \tag{55}$$

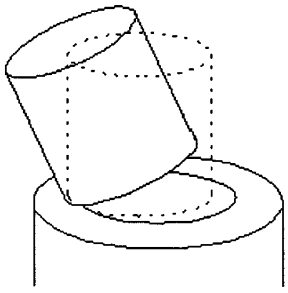


Fig. 24. Left-side angular misalignment.

https://doi.org/10.1017/S026357479900185X Published online by Cambridge University Press

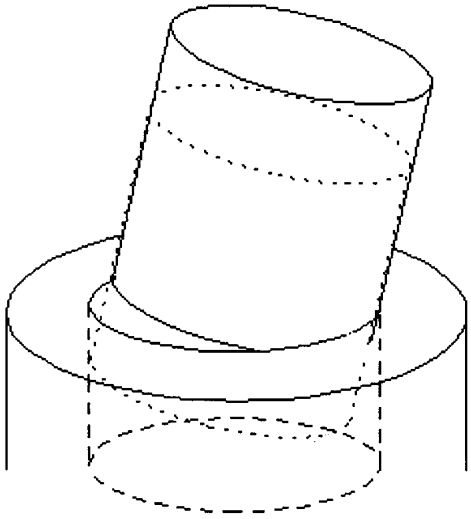


Fig. 25. The peg is in transition from one-to-two point contact.

Putting the relations of eq. (55) into eq. (54), the system dynamic equation is then

$$F_{in(t)} = m\frac{d^2z}{dt^2} + 2\mu K_X e_x \tag{56}$$

In eq. (56), the input is F_{in} and the output z is the insertion depth during the one point contact; to find z, eq. (56) should be transferred by the Laplace transform method, then

$$\begin{aligned} F_{in(s)} &= ms^2 Z_{(s)} + 2\mu K_X e_x \\ Z_{(s)} &= (F_{in(s)} - 2\mu K_X e_x)\frac{1}{ms^2} \end{aligned} \tag{57}$$

The simulation diagram that describes this sub-process (eq. 57) is shown in Figure 27.

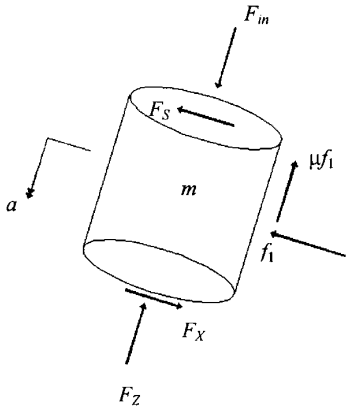


Fig. 26. The FBD of the peg during transition stage.

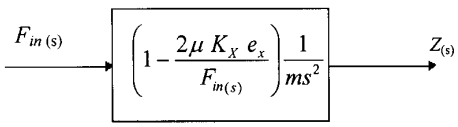


Fig. 27. Simulation block diagram for the peg during one-point contact sliding.

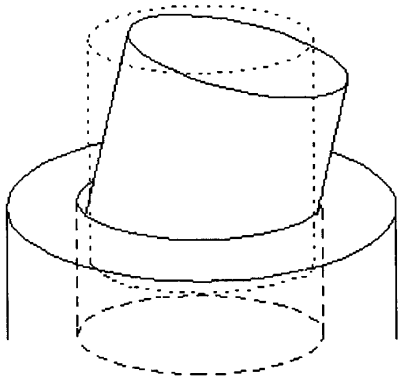


Fig. 28. The peg tilting from two-point contact to zero angular misalignment.

5.5 Final Alignment

Finally, there is a stage where the peg is in two-point contact with the hole (Figure 28).

The input is the torque generated by the reaction forces due the two-point contact. The output is the angular alignment, where the misalignment $\vartheta = 0$. It is assumed that once the peg is inside the hole with a zero angular error, then the insertion process is successfully accomplished.

As before, on the FBD of the peg (Figure 29), the forces acting on it lie in one plane. The system equation is:

$$T_{(t)} - 2T_{S(t)} = I\frac{d^2\vartheta}{dt^t} \tag{58}$$

where $T_{(t)}$ is the input and ϑ is the output of the system.

In eq. (58), the springs torque, $T_{(S)}$, is multiplied by 2; the reason for that is that there are two rotational springs in that plane ($K_{\vartheta X}$ and $K_{\vartheta Z}$, see Figure 18). The input $T_{(t)}$ is equal to

$$(rF_Z\left[\frac{1}{2r\mu} - \frac{F_X}{F_Z}\left(\frac{1}{2r} + \mu\right)\right]).$$

Note that l is the output z from the previous stage.

Rearranging eq. (58) and then transferring by the Laplace transfer method,

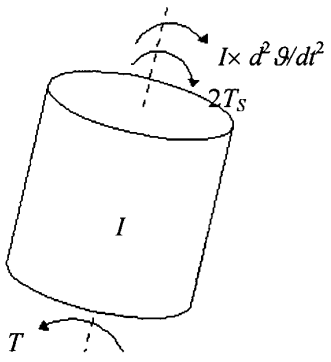


Fig. 29. Rotational forces acting on the FBD of the peg during two-point contact.

https://doi.org/10.1017/S026357479900185X Published online by Cambridge University Press

$$T_{(t)} = I\frac{d^2\vartheta}{dt^2} + 2K_\vartheta\vartheta$$
$$T_{(s)} = Is^2\vartheta + 2K_\vartheta\vartheta$$
$$\frac{\vartheta_{(s)}}{T_{(s)}} = \frac{1}{Is^2 + 2K_\vartheta} \quad \text{or} \quad (59)$$
$$\vartheta_{(s)} = T_{(s)}\frac{1}{Is^2 + 2K_\vartheta}$$

To complete the insertion process, the output ϑ (in eq. 59) has to become zero. This is achieved when the springs/wrist tilt the peg to the other side until contact between the mating parts is broken from both sides, when no reaction forces exist any more. Also, it is assumed that once the peg is inside the hole and no contact exists, peg sliding could continue till the desired insertion depth without risking a jamming/wedging occurrence.

The simulation block diagram that describes the final stage of the insertion process i shown in Figure 30.

6. SIMULATION

A simulation programme (Matlab-Simulink) was designed to simulate the peg-in hole insertion process (Figure 31). The principles of this programme are the same as those for Figure 15. The input is a signal generator which provides the system with a constant square signal to run the transfer function blocks that had been derived from the mathematical models of the insertion process. The signal is defined as an applied force. The scope blocks throughout the programme are to monitor the progress of the simulation process. If there is a lateral transition and/or angular tilt, the driving signal is fed to the appropriate block. The signal leaves that block and is fed to a summing junction in a negative form to minimise that error. This process is repeated until the signal or the force driving the peg into the hole encounters no misalignments (end of the simulation process). By changing the values of the applied force and the parameters of this programme, different results could be obtained.

Figure 32 is a summary of the results obtained during the simulation process.

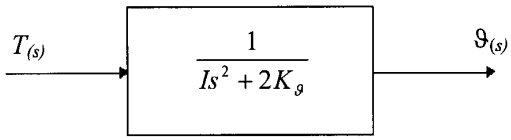


Fig. 30. Simulation block diagram for the peg during tow-point contact-completion stage.

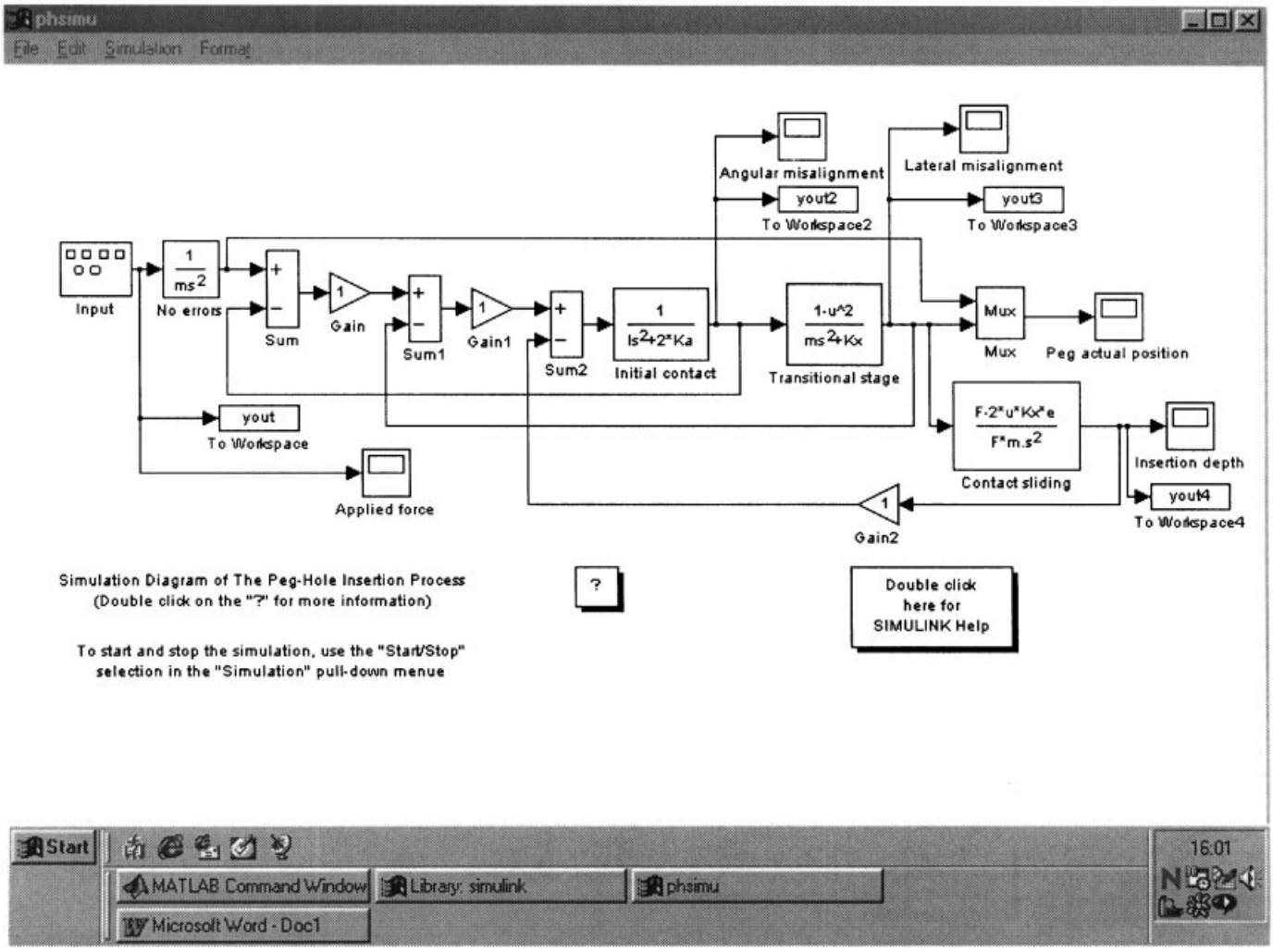


Fig. 31. Simulation diagram for the peg-in-hole insertion process.

https://doi.org/10.1017/S026357479900185X Published online by Cambridge University Press

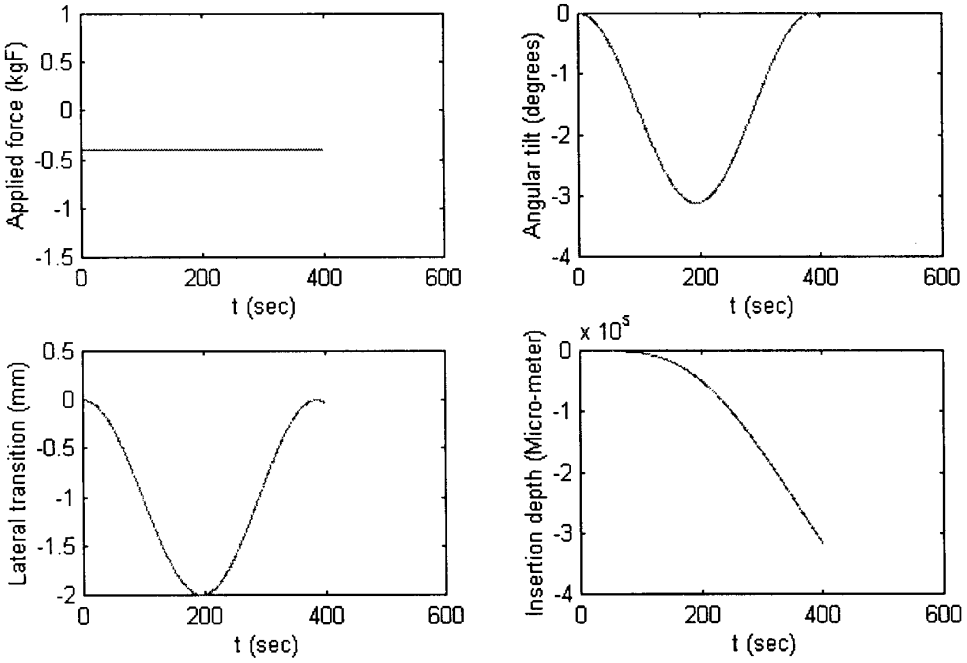


Fig. 32. Summary of simulation results.

7. CONCLUSION

In this paper, a study of the geometrical and dynamical conditions for a successful insertion process has been presented. Following that, a mathematical model has been derived and simulated using Matlab-Simulink software. The results of this research would form a tool for designing or optimising assembly strategies and/or devices of both passive and active methodologies.

References

1. T. Tsuruoka, H. Fujioka, T. Moriyama and H. Mayeda, "3D Analysis of Contact In Peg-Hole Insertion", *Proceedings of the 1997 IEEE Int. Symp. on Assembly and Task Planning*, Marina del-Rey, CA USA, (August 1997) pp. 84–89.
2. R.E. Gustavson, "A Theory For The Three Dimensional Mating Of Chamfered Cylindrical Parts", *Trans. of ASMEE*112 **107**, 113–123 (March, 1985).
3. H. Qiao, B.S. Dalay and R.M. Parkin, "Precise Robotic Chamferless Peg-Hole Insertion Operation Without Force Feedback And Remote Centre Compliance", *Proc. of the Inst. of Mech. Engrs.* **208**, 89–104.
4. G. Arz Kiss, A. Lazar and A.Z. Toth, "Dynamic Analysis Of The Peg-Hole Insertion With Stick-Slip Friction And Impact", *7th Int. Daaam Symp.*, Technical University of Vienna (17–19 October, 1996).
5. H. Zohoor and M. Shahinpoor, "Dynamic Analysis Of Peg-In-Hole Insertion For Manufacturing Automation", *J. Manufacturing Systems* **10**, No. 2, 99–108 (1984).
6. D. Whitney, "Quasi-Static Assembly Of Compliantly Supported Rigid Parts", *ASME J. Dyn. Syst. Meas. Contr.* **104**, 65–77 (1982).
7. W. Haskiya, K. Maycock and J.A.G. Knight, "A Passive Compliant Wrist Fro Chamferless Peg-In-Hole Assembly Operation From Vertical and Horizontal Directions", *Proc. Inst Mech Engrs.* **212**, Part B, 473–478 (1998).
8. M.T. Mason, "Compliant Motion", *Robot Motion-Text Book* MIT Press, Cambridge, Massachusetts and London, 305–332 (1983).
9. R. Setchi and D. Bratanov, "Three-Dimensional Simulation Of Accommodation", *Assembly Automation* **18**, No. 4, 291–301 (1998).
10. Y. Wang and M. Mason, "Modelling Impact Dynamics For Robotic Operation", *Proc. Of the 1987 IEEE Int. Conf. on Robotics and Automation* 1987), pp. 678–685.
11. R. Featherstone, "The Dynamics Of Rigid Body Systems With Multiple Concurrent Contact", *The Third Int. Symp.*, Cambridge MA Internet version.
12. M. Erdman, "On A Representation Of Friction In Configuration Space", *Int. J. Robotics Research* **13**, No. 3, 240–271 (June, 1994).
13. D. Whitney, "Part Mating In Assembly", *Handbook of Industrial Robotics* John Wiley & Sons, USA (1985), pp. 1084–1186.

https://doi.org/10.1017/S026357479900185X Published online by Cambridge University Press